JOURNAL OF PROPULSION AND POWER
Vol. 16, No. 3, May–June 2000

Transverse Injection from Circular and Elliptic Nozzles into a Supersonic Crossflow

M. R. Gruber* and A. S. Nejad†
U.S. Air Force Research Laboratory, Wright–Patterson Air Force Base, Ohio 45433
T. H. Chen‡
Taitech, Inc., Beavercreek, Ohio 45431
and
J. C. Dutton§
University of Illinois at Urbana–Champaign, Urbana, Illinois 61801

An investigation of sonic transverse injection from circular and elliptic nozzles into a supersonic crossflow using planar Rayleigh/Mie scattering is reported. Instantaneous images allow examination of the structural details, whereas ensemble-averaged images provide transverse penetration and lateral spread data for each jet. Standard deviation images produce information regarding the large-scale mixing/entrainment and reveal the mixing zones. Results show a highly three-dimensional near-field interaction dominated by shear-layer eddies and a counter-rotating vortex pair. Ensemble-averaged results show that the elliptic jet spreads more rapidly in the lateral direction than the circular jet, confirming that an axis-switching phenomenon is present. Near-field transverse penetration data collapse well with low-speed scaling conventions; however, the jet produced by the elliptic nozzle suffers a 20% reduction in penetration compared to the circular jet. Compressibility level does not play a significant role in the average penetration or spread of these jets, although it strongly affects the mixing/entrainment and large-scale structure. Analysis of mixing potential from the standard deviation images indicates that the low and high convective Mach number M_c injection cases are significantly different; low M_c injection yields better large-scale mixing potential than high M_c injection regardless of the injector geometry.

Nomenclature

A	= area
a	= semimajor axis; 3.18 mm for circular; 6.25 mm for elliptic; speed of sound
b	= semiminor axis; 3.18 mm for circular; 1.63 mm for elliptic
d_{eff}	= effective diameter, $2(A_{\text{xs}}/\pi)^{0.5}$; 6.35 mm for circular and elliptic
J	= jet-to-freestream momentum flux ratio, $(\gamma p M^2)_j/(\gamma p M^2)_\infty$
M	= Mach number
M_c	= convective Mach number
P	= perimeter
p	= static pressure
p_0	= stagnation pressure
R	= area ratio
Re	= Reynolds number
r_0	= effective radius, $(A_\sigma/\pi)^{0.5}$
S	= large-scale shape parameter, $P/2\pi r_0$
T_0	= stagnation temperature
u	= velocity
x, y, z	= streamwise, transverse, and spanwise coordinates
γ	= specific heat ratio
$\Delta x, \Delta y, \Delta z$	= streamwise, transverse, and spanwise pixel dimensions
δ	= boundary layer thickness
ε	= eccentricity, $[1-(b/a)^2]^{1/2}$; 0 for circular; 0.97 for elliptic
μ	= dynamic viscosity
ρ	= density
σ	= standard deviation
σ_{norm}	= normalized standard deviation
$\bar{\sigma}_\infty$	= average freestream standard deviation

Subscripts

i	= pixel x location
j	= jet exit property, pixel y location
xs	= nozzle cross section
σ	= standard deviation
90	= 90% contour
∞	= freestream

Received 4 February 1998; revision received 10 April 1999; accepted for publication 4 May 1999.

*Aerospace Engineer, Propulsion Sciences and Advanced Concepts Division, High Speed Systems Development Branch, Building 18. Senior Member AIAA.

†Aerospace Engineer, Propulsion Sciences and Advanced Concepts Division, High Speed Systems Development Branch, Building 18; currently Director of Engineering, Kaiser Marquardt, 16555 Saticoy Street, Van Nuys, CA 91406. Member AIAA.

‡President, Suite H, 2372 Lakeview Drive. Member AIAA.

§W. Grafton and Lillian B. Wilkins Professor, Department of Mechanical and Industrial Engineering. Associate Fellow AIAA.

Introduction

EFFICIENT injection, mixing, and reaction processes that occur inside a supersonic combustion chamber will be fundamental to the success of airbreathing hypersonic vehicles. These processes must take place in a supersonic stream because of undesirable effects associated with decelerating a supersonic flow ($M = 6$–8) to appropriate speeds for subsonic combustion. Residence times within such combustors will necessarily be short, thus requiring the mixing and combustion to occur rapidly. The work reported herein examines transverse injection through two different injector geometries into a supersonic crossflow. A schematic of the transverse jet injected into a supersonic crossflow appears in Fig. 1. This scheme represents one possible arrangement for fuel injection in supersonic combustors. A three-dimensional bow shock forms ahead of the injectant stream and interacts with the approaching boundary layer, resulting in a separation bubble. A barrel shock also occurs as the underexpanded jet accelerates into the crossflow. Acceleration of the jet core continues until a normal shock (or Mach disk) forms. Downstream of

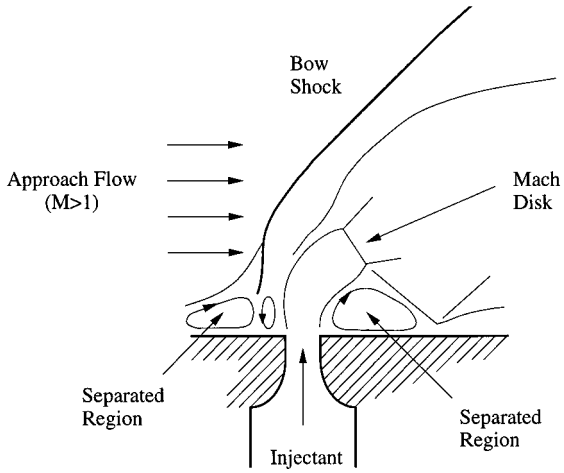

Fig. 1 Transverse injection flowfield schematic.

the jet plume a second separated zone develops between the jet exit and the boundary-layer reattachment point.

Fric and Roshko[1] conducted an experimental study of large-scale structures in subsonic transverse injection flowfields. They found four types of vortical structures near the injector exit: shear-layer vortices, a counter-rotating pair, horseshoe vortices, and a wake vortex system. The shear-layer vortices developed from vorticity in the jet boundary layer and rolled up into the freestream fluid. The counter-rotating pair, which also formed from vorticity in the jet boundary layer,[2] was streamwise-oriented and relatively two-dimensional.[3] Horseshoe vortices form in the near-wall region from vorticity within the crossflow boundary layer and vorticity generated caused by the wall pressure gradient resulting from the jet/freestream interaction. The most interesting findings of Fric and Roshko[1] were the wake vortices. Previous vortex shedding measurements acknowledged the presence of such structures,[4] but the dynamics of their formation and their characteristic motions were unknown. Fric and Roshko[1] found that the jet's vorticity did not contribute to the development of wake vortices; rather, these structures formed from vorticity present in the crossflow boundary layer. They also showed a dramatically different wake structure compared to that created by a solid body in the crossflow.

Fundamental investigations of the vortex structure of wall injection into a supersonic flow are less common. Heister and Karagozian[5] proposed a model of the flow based on the dominant counter-rotating vortex pair formed within the jet. Other experimental[6–9] and numerical[10,11] studies of basic and more complex injection geometries consistently document the presence of these characteristic vortices. However, the freestream and jet shock structures, along with the time-averaged features of the flow, received more attention than this vortex pair. Studies using laser-based diagnostics[9,12–14] revealed large eddies present within the shear layer at the jet/freestream interface. These vortices contributed significantly to near-field entrainment. Oil-flow studies[11,14] show the horseshoe vortex region, and recent evidence of wake vortices is also available.[15]

Circular and noncircular nozzles produce jets exhibiting very different structural characteristics in the presence of both quiescent and coflowing environments.[16–21] Small aspect ratio elliptic jets have an asymmetric boundary-layer momentum thickness distribution around the circumference of the jet orifice.[16] An instability develops from the maximum vorticity associated with the smallest momentum thickness,[17] leading to asymmetric vortices shedding from around the nozzle exit. As a result of this asymmetry, the spreading characteristics in the major and minor axis planes are very different. At some point downstream of the nozzle exit, depending on the aspect ratio of the nozzle, the major and minor axes have equal widths. Farther downstream, an axis switch occurs as the spreading of the minor axis plane overtakes that of the major axis.[18,19] This minor axis spreading is significantly greater than the spread associated with a circular jet, where symmetric vortices form at the nozzle exit. Underexpanded elliptic jets spread faster than perfectly expanded or subsonic elliptic jets because of acoustic feedback from the large structures in the shear layer.[22] Similar feedback effects in circular underexpanded jets result in vortical mode changes within the jet and alterations of the near-field pressure fluctuations rather than in spreading enhancement.[20] Recently, Gruber et al.[23,24] have presented some evidence that jets issuing from elliptic and circular nozzles into a supersonic crossflow behave differently. Their results show an influence on both the convection of the shear layer eddies and the characteristics of the upstream bow shock and separation region.

The objective of the current work is to obtain a more thorough understanding of the dominant features that govern near-field mixing in flowfields created by transverse injection from circular and elliptic nozzles into supersonic streams. As suggested by the results just discussed, large-scale motions and injector geometry strongly influence the near-field mixing processes in these flows. By using a planar imaging technique in the near field, more insight into the fundamental fluid dynamic mechanisms of the jet/crossflow interaction is obtained. Relevant data include transverse penetration and lateral spread, as well as statistics concerning the streamwise vortex pair, large-scale shear layer structures, and near-field mixing.

Experimental Facility

The experiments documented herein were performed in the supersonic research facility located at Wright-Patterson Air Force Base. The various components of this facility have been discussed in detail elsewhere[25]; a summary of the important features is included.

Flow Facility

A continuous supply of pressurized air enters the inlet section of the test apparatus and flows into the settling chamber. This section houses flow conditioning devices and sensors for measuring the stagnation pressure and temperature of the freestream. The air then accelerates in the two-dimensional nozzle section to a nominal Mach number of 2 before entering a constant area test section (cross-section dimensions of 131 × 152 mm). Several fused silica windows placed in the test-section walls allow for nonintrusive investigations of the flowfield. Two injectors (circular and elliptic cross sections) were incorporated into the test section. The details of the injector designs appear elsewhere[9]; geometric features are found in the Nomenclature. The elliptic nozzle major axis was aligned with the crossflow. Both injectors were placed at the same streamwise location to ensure that the crossflow boundary-layer thickness approaching the jet would be the same for each ($\delta/d_{\text{eff}} = 1$) (Ref. 25). A pressure tap near each jet exit measured static pressure and a thermocouple in the supply line measured stagnation temperature. Two dry gases supplied each nozzle (air and helium) allowing two convective Mach numbers to be studied.[15,24]

Imaging System

Two optical arrangements were used for flowfield interrogation. A Spectra Physics Quanta-Ray DCR-4 Nd:YAG laser (532 nm, 400 mJ/pulse) provided the laser energy, and a combination of mirrors, prisms, and lenses produced the collimated laser sheet used for illuminating the flowfield. The sheet (50 mm wide and 200 μm thick) entered the test section through a side window (end view) or the top window (side view). A Princeton Instruments ICCD camera (384 × 576 pixel array) and image acquisition system obtained the flowfield images. The camera was water-cooled and purged with nitrogen to reduce dark current noise.

Seeding Issues and Technique

Details of the particle seeding technique used in these experiments have been previously documented.[15,24] In summary, silane (SiH_4) combustion produced the seed particles that marked freestream fluid. Silane is a pyrophoric gas that, when exposed to oxygen, burns to form primarily solid silicon dioxide (SiO_2), water, and hydrogen.[26] The particles produced in this reaction were characterized as having diameters in the 0.2 μm range.[27] By themselves, these particles have

Table 1 Experimental conditions

Case	CA	CH	EA	EH
γ_∞, γ_j	1.40, 1.40	1.40, 1.67	1.40, 1.40	1.40, 1.67
$p_{0,\infty}$, $p_{0,j}$, kPa	317, 902	317, 832	317, 902	317, 832
$T_{0,\infty}$, $T_{0,j}$, K	302, 300	300, 300	302, 300	300, 300
M_∞, M_j	1.98, 1	1.98, 1	1.98, 1	1.98, 1
$Re_\infty = (\rho u)_\infty / \mu_\infty$, m^{-1}	3.87×10^7	3.91×10^7	3.87×10^7	3.91×10^7
$Re_j = (\rho u d)_j / \mu_j$	8.36×10^5	3.00×10^5	8.36×10^5	3.00×10^5
J	2.90	2.93	2.90	2.93
M_c	0.66	1.92	——[a]	——[a]

[a]The model used to estimate M_c does not extend to noncircular geometries[15]; thus, no estimates are included.

Stokes numbers, defined as the ratio of the particle response time scale to the characteristic fluid dynamic timescale, of 0.09. This falls well below the criterion established by Samimy and Lele[28] for accurate particle response for Mie scattering images (i.e., Stokes number ≤ 0.5). However, because of the natural moisture present in the crossflow air supply, ice formed around these small particles as the freestream flow expanded in the Mach 2 nozzle. This resulted in larger particles and higher Stokes numbers. These combined SiO_2/ice particles were found to be in the Rayleigh scattering regime at 532 nm and thus had maximum Stokes numbers of about 0.4. Because of the presence of water vapor and the varying thermodynamic conditions throughout the jet/freestream interaction, the diagnostic technique used in this investigation produces no direct measurements of injectant number density.

Results and Discussion

Flow conditions for the present investigation appear in Table 1. Four conditions are considered with air and helium each supplied to the circular (cases CA and CH) and elliptic (cases EA and EH) injectors. When using helium as the injectant, the compressibility of the jet-freestream shear layer is quite high ($M_c = 1.92$) as compared to the air cases ($M_c = 0.66$). The jet-to-freestream momentum flux ratio remains constant for all experiments. The results that follow are separated into those from end- and side-view imaging arrangements. All of the image color scales have been reversed such that the seeded crossflow fluid appears dark while the unseeded jet fluid appears light; this highlights the features within the jet.

End-View Images

By visualizing the transverse injection flowfield from the end, the cross-sectional structure of the jet is observed. Additionally, as the image plane moves downstream, the near-field development of the interaction may be examined. All of the images presented in this section have pixel dimensions $(\Delta x, \Delta y, \Delta z) = (200, 90.7, 90.7\,\mu\text{m})$, and the flow direction is out of the plane of the paper. Each end-view image covers about 6.4 diameters (40.6 mm) in the spanwise (z) direction and 5.4 diameters (34.3 mm) in the transverse (y) direction. Also, each image has been corrected for the off-axis nature of the camera orientation. Ensembles of either 20 or 100 images were obtained (20 shots at $x/d_{\text{eff}} = 0$ and 8; 100 shots at $x/d_{\text{eff}} = 4$ and 10).

Instantaneous Images

Figure 2 shows instantaneous images of the four cases from streamwise positions $x/d_{\text{eff}} = 0, 4$, and 8. Images taken with the laser sheet positioned at the jet centerline (i.e., $x/d_{\text{eff}} = 0$) show the shape of the bow shock the three-dimensional nature of the flow. Also prominent in the images from this location are the large-scale eddies that form in the interfacial region between the jet and freestream fluids. These structures form at the earliest stages of the interaction. Another important feature at $x/d_{\text{eff}} = 0$ is that the lateral spread of the jets created by the elliptic and circular nozzles are nearly equal despite the elliptic nozzle having a minor axis that is half that of the circular nozzle. As the image plane moves downstream, the vortical structure in the jet fluid becomes more apparent. Each case studied here shows significant large-scale behavior at $x/d_{\text{eff}} = 4$. Counter-rotating vortices emerge as the jets elevate off the tunnel floor. The

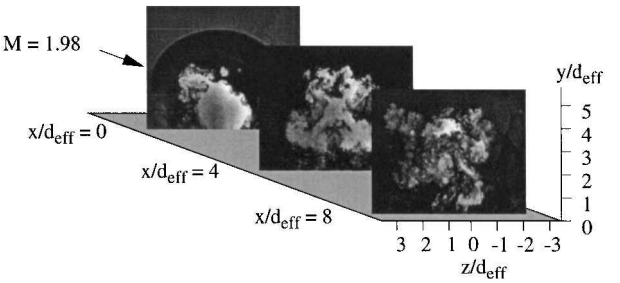

a) Case CA

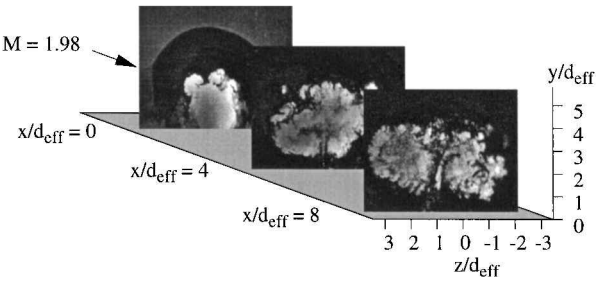

b) Case CH

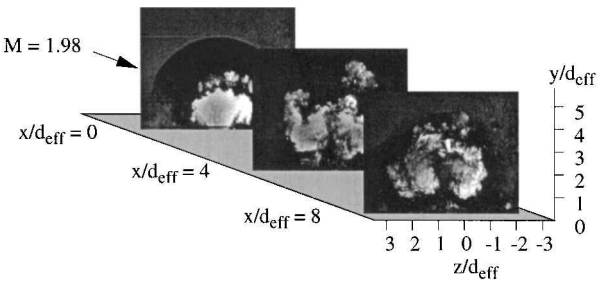

c) Case EA

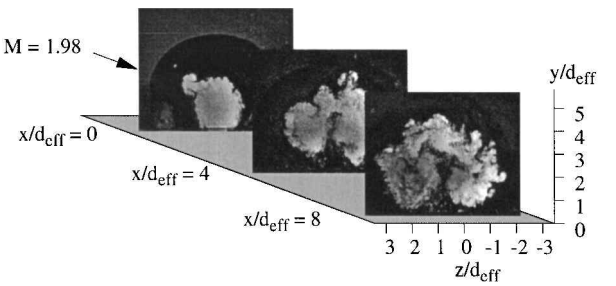

d) Case EH

Fig. 2 Instantaneous end-view images.

edges of the jet fluid appear convoluted and dominated by large- and small-scale vortices. By $x/d_{\text{eff}} = 8$ the jets in the air injection cases (CA and EA) have begun to break up, while the helium cases (CH and EH) appear more coherent.

Ensemble-Averaged Results

Ensemble-averaged images were analyzed for jet spread (Fig. 3a) and plume area (Fig. 3b). The jet edge is defined as the location of an intensity that is 90% of the average freestream intensity behind the bow shock. This provides a boundary between essentially pure freestream fluid and fluid at some intermediate mixture fraction. This technique adequately describes the outer jet edge.[9] Error bars are indicative of ±10 pixel (±0.91 mm) uncertainty in the determination of the jet edge.

In Fig. 3a the lateral spread data are normalized by the nozzle minor axis. The circular nozzle cases show comparable spreading characteristics to $x/d_{\text{eff}} = 4$. Beyond this location, a small degree of contraction in the jet occurs. This is actually indicative of crossflow fluid being entrained into the jet fluid (i.e., that the jet fluid is stirred with the seeded crossflow fluid, yielding smaller regions containing high injectant concentrations). Case CH appears to contract slower than case CA, leading to the conclusion that the relatively higher mixing-layer compressibility level in case CH results in slower entrainment of freestream fluid into the jet. The elliptic nozzle cases show similar trends regarding the influence of compressibility on entrainment into the jet. However, the jets issuing from the elliptic nozzle spread markedly further laterally into the crossflow relative to the nozzle minor axis dimension than the jets from the circular nozzle. This observation provides strong evidence that the axis-switching phenomenon observed in other elliptic nozzle studies is preserved in this configuration.[18,19]

The area enclosed by the 90% intensity contour (A_{90}) yields more information regarding the entrainment characteristics of the jets. Figure 3b shows the results of computing the enclosed area normalized by the exit area of the injector. The plot reveals two separate trends. Both air injection cases (low M_c) indicate increasing areas to approximately $x/d_{\text{eff}} = 4$. Beyond this location, the areas decrease sharply. In the helium injection cases (high M_c) the area increases beyond $x/d_{\text{eff}} = 4$ with reductions occurring farther downstream than for cases CA and EA. The area enclosed by the 90% contour becomes smaller as the amount of freestream fluid within the jet region increases. Thus, the sharp reductions in area for the low M_c cases between $x/d_{\text{eff}} = 4$ and 8 suggest an increased amount of freestream fluid in the jet region as compared to the high M_c cases CH and EH. From this analysis compressibility strongly influences the entrainment characteristics with high M_c acting to reduce entrainment of freestream fluid into the jet regardless of injector geometry.

Standard Deviation Results

Standard deviation images appear in Fig. 4 for each case studied. These images were rescaled and normalized using

$$\sigma_{\text{norm}_{i,j}} = |1 - \sigma_{i,j}/\bar{\sigma}_{\infty}| \tag{1}$$

such that the intensity values range from $\sigma_{\text{norm}} = 0$ (black) in the unfluctuating freestream and jet cores to values approaching $\sigma_{\text{norm}} = 1$

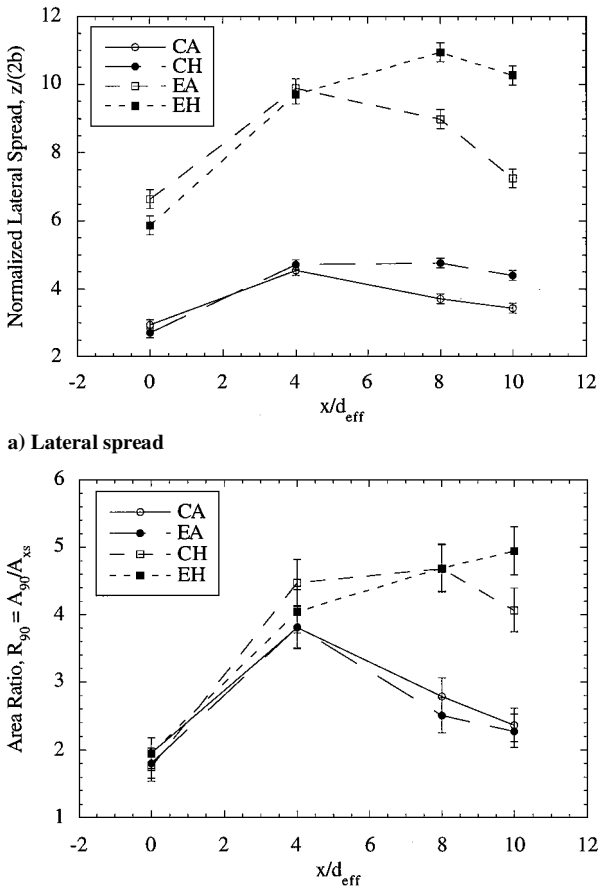

Fig. 3 End-view ensemble-averaged results.

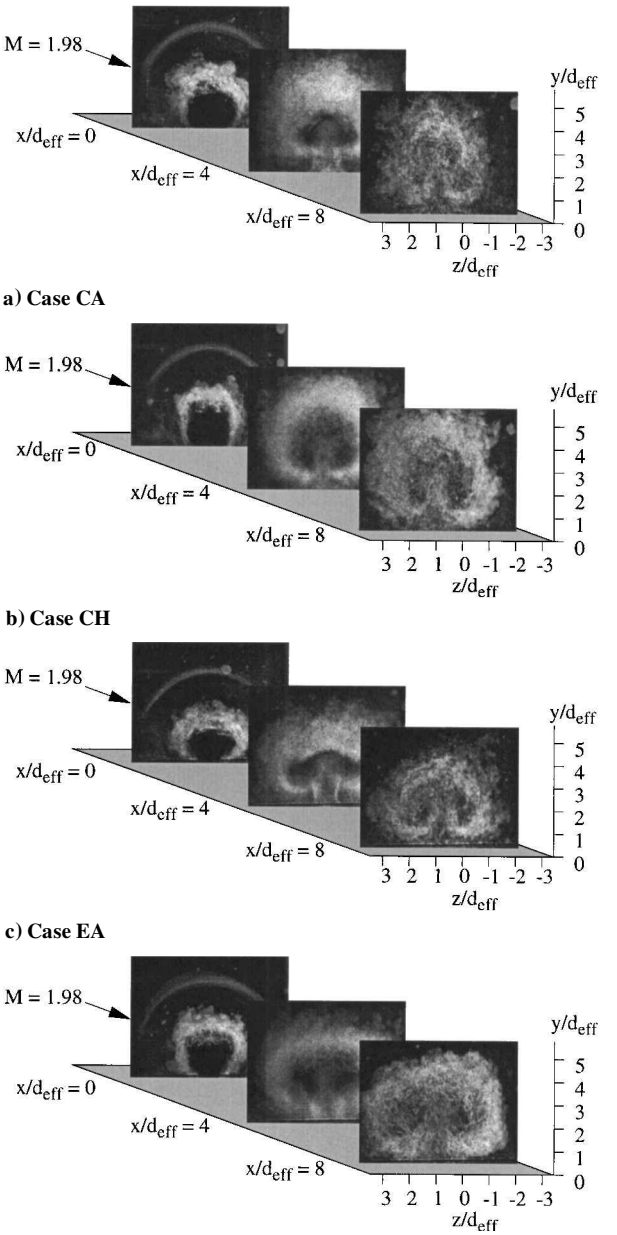

Fig. 4 Normalized standard deviation end-view images.

(white) in the shear layers. The signal fluctuations used in Eq. (1) were significantly greater than any intensity fluctuations caused by system noise.

At $x/d_{\text{eff}} = 0$ the bow shock fluctuates slightly as indicated by the light region arcing above the jet. This is consistent with results published earlier showing the bow shock being influenced by the large-scale eddies intermittently formed at the jet's upper edge.[23] The shear-layer region around the periphery of the jet is also observed. Thus, most of the freestream entrainment that occurs at this location does so because of the large-scale eddies evolving at the upper edge of the jet. Also apparent are the undisturbed jet cores and crossflow.

Moving downstream to $x/d_{\text{eff}} = 4$, the development of the mixing region around the periphery of the jet can be examined more closely. Here, the region of fluctuating fluid has grown substantially around the jet. Note the region between the two counter-rotating vortices near the bottom wall where significant entrainment occurs. Also note that the central cores of the two counter-rotating vortices remain relatively devoid of fluctuating fluid compared to the region surrounding them. Thus, some regions of unmixed fluid (in terms of the turbulent fluctuations) still exist. In the high compressibility cases [i.e., cases CH (Fig. 4b) and EH (Fig. 4d)], the jet cores remain relatively large while the enclosing shear layer is relatively thin compared to the images from cases CA and EA. Comparing circular and elliptic injection cases reveals that the jets from the elliptic nozzle are wide and flat with the counter-rotating vortices being farther apart than those that develop in the jets from the circular nozzle. This widening of the vortices allows more freestream fluid to be entrained into the central core. VanLerberghe[19] found the best mixing performance in a similar flowfield to occur below and between these vortices. Thus, passively or actively enhancing the effectiveness of this vortex pair may lead to significantly better overall mixing characteristics. Similar features are observed at $x/d_{\text{eff}} = 8$, although the jet cores appear more incoherent in cases CA and EA.

To quantify the large-scale mixing characteristics of the four cases studied here, an arbitrary contour ($\sigma_{\text{norm}} = 0.30$) was chosen to yield a quantitative representation of the region containing fluctuating fluid. Inside this contour fluid is either engaged in large- or small-scale mixing. Because small-scale mixing occurs at length scales smaller than those discernible with the current pixel resolution, no differentiation can be made between the two processes. However, it is reasonable to expect that the chosen contour encloses essentially the entire mixing region and can therefore be characterized as to its mixing potential, because all of the fluid within the contour has the potential to become molecularly mixed. Once obtained, the area enclosed within the contours A_σ and their perimeters P were computed. A shape parameter S, defined by

$$S = P/2\pi r_0 \qquad \text{where} \qquad r_0 = \sqrt{A_\sigma/\pi} \tag{2}$$

was then used in conjunction with A_σ to indicate the degree of mixing potential afforded by the injection scheme. This shape parameter has been used in a recent investigation of parallel injection into a supersonic stream with good success.[29] This parameter describes the relationship between the perimeter and area of a given contour and compares them to a perfectly circular contour. If the contour of interest were a perfect circle, the value of S produced would be unity. This is also the geometry that leads to a minimum value of the shape parameter just defined. Thus, contours with shape parameters greater than unity have greater mixing potential than those having values of S near unity by virtue of increased interfacial mixing area and the presence of large-scale structure.

Plots of the area and shape parameter for the four cases appear in Fig. 5. As in Fig. 3, error bars are indicative of ±10 pixel uncertainty in determining the jet edge. Some very distinct trends can be found in these data. First, Fig. 5a shows the area ratio resulting from the analysis, where this ratio is defined as the area inside the standard deviation contour A_σ, divided by A_{90}. Two distinct pairs of curves result. All cases show increasing values of R_σ with increasing downstream distance. However, values of R_σ from the low M_c cases are always larger than those from the high M_c cases. From the plot in Fig. 5a, one can observe that the effects of injector geometry on the area within the mixing contour are relatively weak compared to the effects of compressibility.

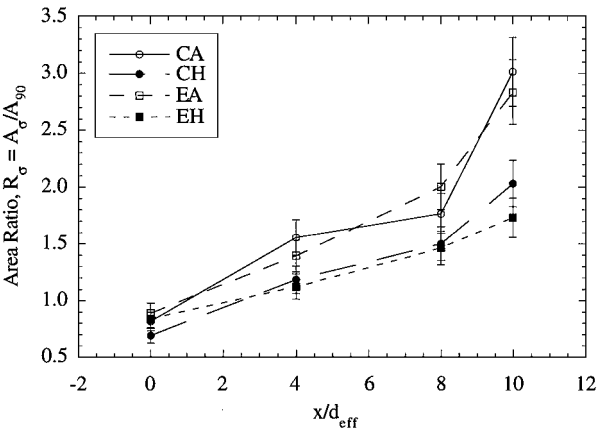

a) Mixing region area ratio

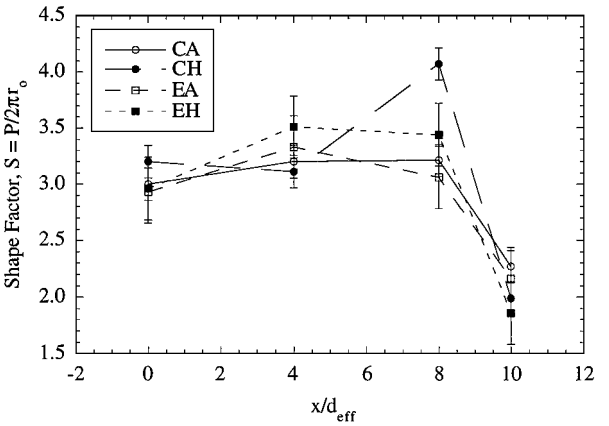

b) Mixing region shape factor

Fig. 5 End-view standard deviation results.

All cases have similar shape factors (Fig. 5b) in that a sharp decay is experienced in the far field ($8 < x/d_{\text{eff}} < 10$). The plateau region in the near field occurs at or above a value of approximately 3, suggesting that the contours are highly convoluted when compared to a perfect circle. The sharp decay indicates that the contours tend to become more circular in the far-field mixing region. Thus, large-scale mixing appears more prominent in the near fields of these injectors. Glawe et al.[29] suggest that the combination of a large shape parameter and a large area indicate favorable mixing characteristics. On the basis of this observation and the data presented in Fig. 5, the low M_c flowfields result in better entrainment and mixing characteristics over the range of study than the high M_c cases.

Side-View Images

Side-view images offer a view of the jet/crossflow interaction at the spanwise centerline of the injector (i.e., $z/d_{\text{eff}} = 0$). The pixel dimensions of the images presented in this section are $(\Delta x, \Delta y, \Delta z) = (87.6, 87.6, 200\,\mu\text{m})$ and the flow direction is from left to right. Each side-view image covers about 5.6 diameters (35.6 mm) in the streamwise x direction and 5.3 diameters (33.7 mm) in the transverse y direction. Ensembles of 100 temporally uncorrelated images were collected from two adjacent streamwise positions.

Instantaneous Images

Figure 6 presents select instantaneous images of cases CA, CH, EA, and EH. These images show the bow shock and, in some cases, the separation shock (left sides of images). Also prominent in the

side-view images are the large-scale eddies that form in the interfacial region between the jet and freestream fluids. Wake vortices are also commonly observed as vertical projections of jet fluid between the lower edge of the jet and the tunnel floor. Differences in jet structure appear depending on the compressibility level of the shear layer. In cases CA and EA, for example, eddies formed at the upper edge of the jet are distinct, large-scale extrusions into the crossflow. These structures appear to entrain freestream fluid into their cores and strain the interface between each other. They become broken as they convect downstream indicating break up. Also, the jet core breaks rapidly downstream of approximately $x/d_{\text{eff}} = 5$. In contrast, the structures found in cases CH and EH are large, coherent, and relatively amorphous. The regions between structures are filamentary compared to those in cases CA and EA, suggesting less entrainment of freestream into the jet. The core of the jet remains coherent as the injectant convects downstream, which further suggests slower entrainment of freestream fluid. Smaller-scale features are more prominent throughout the interface in these two cases. Together these results further indicate that the large-scale structural development in transverse injection flowfields is strongly dependent

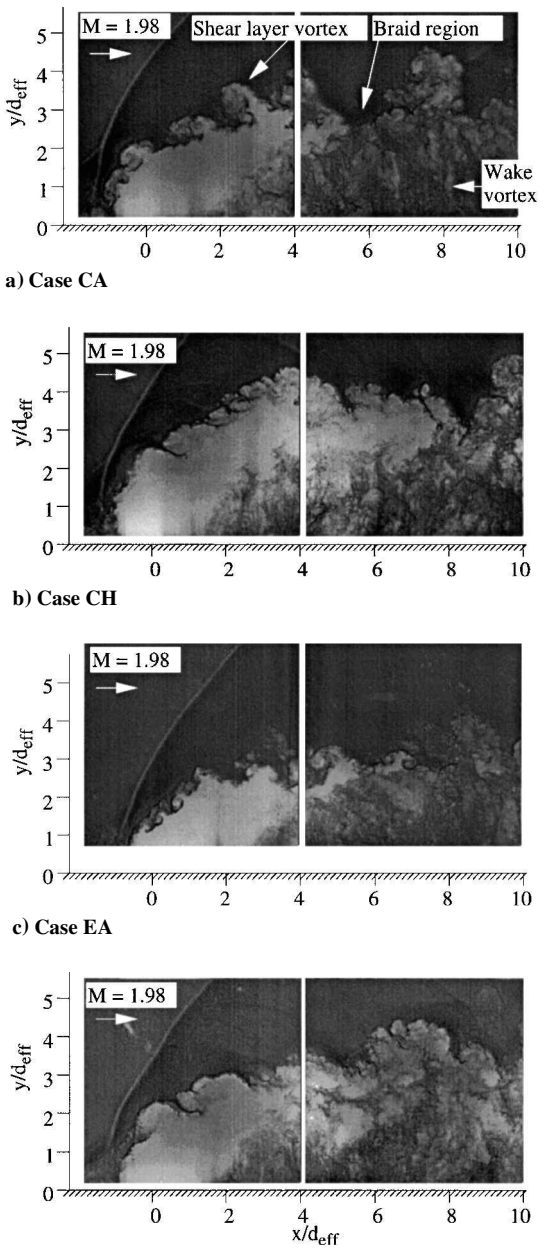

Fig. 6 Instantaneous side-view images.

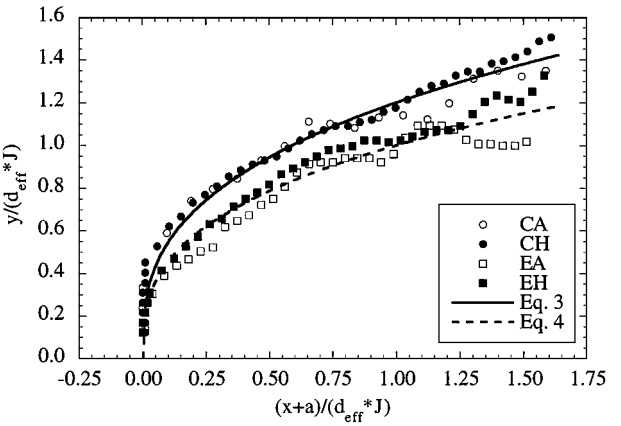

Fig. 7 Transverse penetration data and resulting correlations.

on shear layer compressibility level[15] and injector geometry plays a secondary role.

Ensemble-Averaged Results

Figure 7 presents transverse penetration results obtained from the ensemble-averaged side-view images. As with the end-view ensemble-averaged data just presented, the penetration boundary shown in Fig. 7 corresponds to 90% of the average freestream intensity downstream of the bow shock. Uncertainty in the jet edge is approximately ±10 pixels (±0.88 mm). In their low-speed transverse injection studies Keffer and Baines[30] found that scaling the coordinate axes with the inverse of J collapsed the near-field penetration data from several conditions. Recent results provided comparable success when this scaling convention was applied to transverse injection into supersonic crossflows[9]; thus, this convention is also applied in this study. The aforementioned uncertainty in the position of the jet edge results in an uncertainty of ±0.05 when the results are scaled in this way. The resulting power law curve fits of the near-field penetration data taken from circular and elliptic nozzles are shown in Eqs. (3) and (4), respectively. These expressions apply only in the regions near the injectors, because y becomes unreasonably large as x continues to increase.

Circular:

$$\frac{y}{d_{\text{eff}}J} = 1.2\left(\frac{x+a}{d_{\text{eff}}J}\right)^{0.344} \tag{3}$$

Elliptic:

$$\frac{y}{d_{\text{eff}}J} = 1.0\left(\frac{x+a}{d_{\text{eff}}J}\right)^{0.344} \tag{4}$$

Injector geometry plays a distinct role in the ability of the jet to penetrate into the crossflow. As evidenced in both the figure and the correlations, the elliptic jet penetrates 20% less than the circular jet. This most likely is a manifestation of the axis switch associated with the elliptic injector. The surface pressure field surrounding the elliptic injector is different from that about the circular nozzle, leading to differences in the effective back pressure about the periphery of the jet and, therefore, the transverse penetration. From the plots in Fig. 7, one can see that compressibility has essentially no effect on the transverse penetration of the jets, because for a given injector, the air and helium penetration curves are similar. The penetration data from the circular nozzle also have been shown to compare well with previous work.[31,32]

Standard Deviation Results

Standard deviation images appear in Fig. 8 for each case studied. These images were rescaled and normalized in the same way as mentioned in Eq. (1). In addition to the images, Fig. 8 presents a series of transverse profiles taken from the images to show the

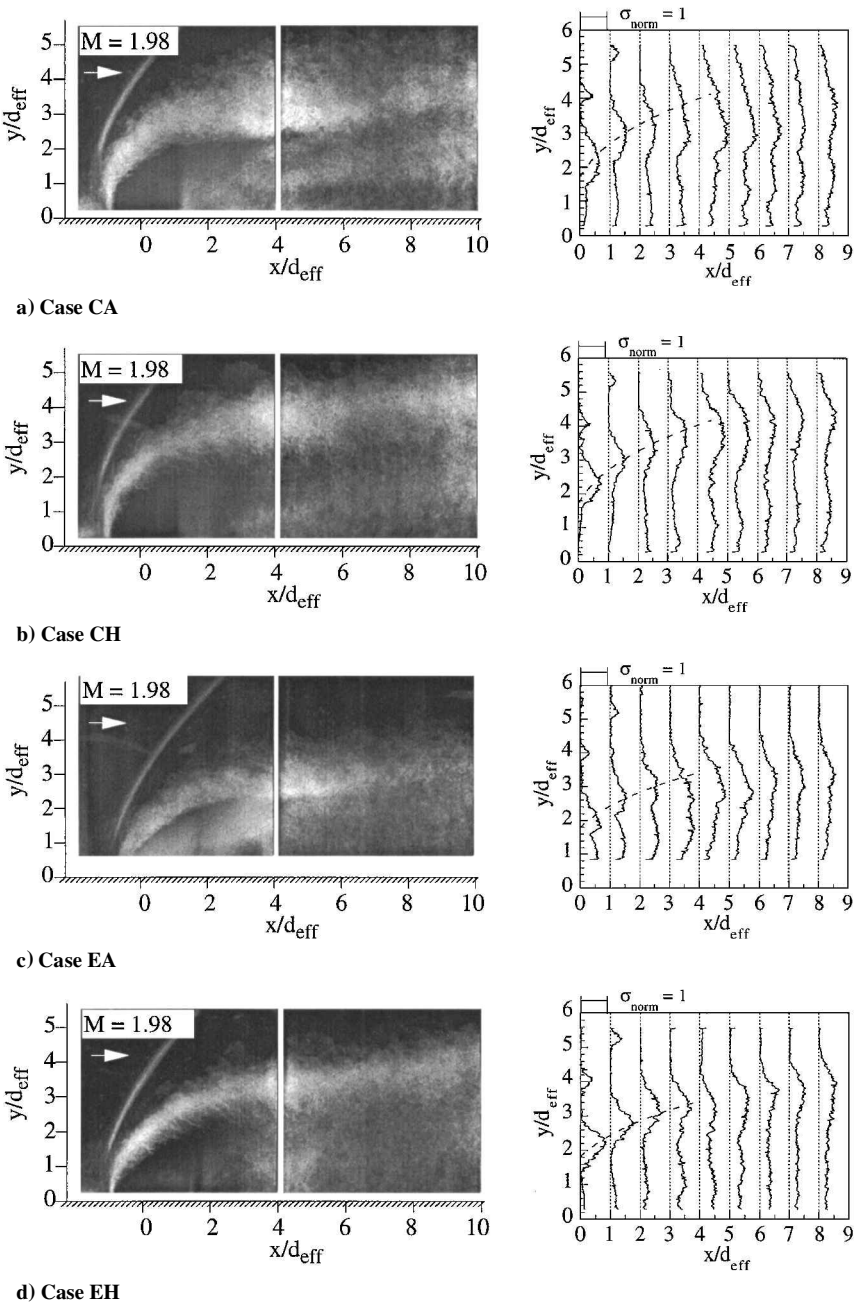

Fig. 8 Side-view standard deviation results.

development of intensity fluctuations from $x/d_{\text{eff}} = 0$–8. Overlaid on these development plots are contours representing the mean upper edge boundaries of the jets [from Eqs. (3) and (4)]. These contours are included to provide a visual marker of the jet boundary.

Each pair of images presented in Fig. 8 illustrates fluctuations in the position of the bow shock. The images also show the development of a shear layer starting from the upstream edge of the injector orifice that grows rapidly as the jet bends because of the momentum of the crossflow. Growth of another shearing region beneath the undisturbed jet core also appears. The two regions of high fluctuations eventually coalesce at the end of the jet core. In cases CH and EH (high M_c), the upper shear layer appears relatively thin compared to the corresponding regions in cases CA and EA (low M_c). Also, the extent of the jet core appears relatively short in the low M_c cases. Beyond the point of coalescence, the entire jet region contains fluctuations.

Bow-shock positional fluctuations appear as standard deviation peaks near $y/d_{\text{eff}} = 4$ and 5 in the first two profiles of each case. These two profiles also show the distribution of normalized fluctuations through the upper shear layer. In each case the first two profiles suggest peaks in fluctuation very near the mean boundary of the jet. Downstream of these two profiles, the bow-shock fluctuations disappear because this feature moves above the measurement domain. However, the growth of the upper-edge mixing region and the development of the lower mixing region can be observed. The profiles downstream of $x/d_{\text{eff}} = 1$ indicate that the location of the peak normalized fluctuation above the jet core is dependent on the compressibility level of the upper shear layer. In cases CA and EA the peak normalized fluctuation occurs well beneath the mean jet boundary. On the contrary, cases CH and EH are characterized by peak fluctuation levels that remain essentially at the jet boundary. Such information suggests that the large-scale eddies which develop in the low convective Mach number shear layers provide deeper entrainment of freestream fluid into the jet than the corresponding structures observed in the high M_c cases. As observed in the instantaneous images, the strained regions between large structures

in cases CA and EA were considerably larger and deeper than the filamentary braid regions found in cases CH and EH. From these observations one can conclude that the entrainment characteristics in the low M_c injection cases are significantly better in the near-field region than in the high M_c cases.

Injector geometry appears to affect the entrainment rate from the lower edge of the jet into the core. In case EA the profiles do not exhibit any bimodal character downstream of $x/d_{\text{eff}} = 4$, whereas in case CA the profiles remain bimodal downstream of $x/d_{\text{eff}} = 8$. Similar remarks can be made about cases EH and CH. Thus, the axis switch occurring in the elliptic injection flowfield may provide enhanced entrainment into the jet from the counter-rotating vortices. As noted in the end-view standard deviation results, any improvement made to the entrainment and mixing performance of these vortices may significantly improve the overall mixing characteristics of the transverse injection scheme.[14] Because injection through an elliptic orifice increases the distance between the counter-rotating vortices, thereby allowing more entrainment of freestream fluid into the jet core, the elliptic geometry may represent an effective passive mixing enhancement scheme.

Conclusions

Transverse injection into a supersonic crossflow through circular and elliptic nozzles has been studied experimentally. The structural details of this three-dimensional flowfield were examined using planar Rayleigh/Mie scattering. Ensembles of images were obtained that provide both end and side views of the interaction. Analyses of these ensembles produce average features (i.e., transverse penetration and lateral spread) along with information concerning the fluctuations and large-scale structures encountered throughout the flowfield.

Instantaneous images reveal information concerning the large-scale structures that develop as the jet and crossflow fluids interact. Large eddies reside in the shear layer at the periphery of the jet, and a counter-rotating vortex pair dominates the jet cross section. Statistical results suggest that the jet issuing from the elliptic nozzle spreads laterally into the crossflow more rapidly than the corresponding circular jet while suffering a 20% transverse penetration reduction. Together, these results suggest an axis-switching phenomenon in the elliptic transverse injection flowfield. The surface pressure fields surrounding the two nozzles are significantly different and may lead to an explanation of this observation. Also, the counter-rotating vortices are farther apart laterally in the elliptic injection cases, thereby providing a larger central entrainment region where freestream fluid may be entrained into the jet core. This region has been shown to be a critical location for entrainment of freestream fluid in transverse injection flowfields. By widening the separation between the counter-rotating vortices, the elliptic nozzle provides this enhancement.

The shear-layer compressibility level strongly influences the large-scale structural characteristics of the jet/crossflow interface and the entrainment characteristics of the jet. However, the compressibility level does not influence the average spread or penetration of the jet. Low-compressibility injection cases yield well-defined structures with large braiding regions as compared to high-compressibility cases, where the eddies are amorphous and the braid regions are thin and filamentary. Rapid break-up of the jet core is observed from the end-view standard deviation images of cases CA and EA (low M_c). Further analysis of these images suggests that the low-compressibility mixing region is larger with respect to the average plume boundary than that of the high-compressibility cases. The shape parameters calculated from the four cases remain similar across the region studied (high in the near-field suggesting large-scale behavior, nearing unity in the far field indicating dominance of small-scale behavior). Statistical results obtained from the side-view images indicate that the fluctuations from the upper-edge shear layer penetrate deeply into the core of the jets in low-compressibility injection cases, whereas those found in high-compressibility cases are confined near the average jet boundary. These observations, coupled with the qualitative results obtained in the instantaneous images, suggest that the low-compressibility injection cases provide greater mixing potential.

Acknowledgments

The contributions of C. Carter, J. Donbar, D. Glawe, D. Schommer, C. Smith, and the support of the Air Force Office of Scientific Research are appreciated.

References

[1]Fric, T. F., and Roshko, A., "Structure in the Near Field of the Transverse Jet," *Seventh International Symposium on Turbulent Shear Flows*, edited by F. Duret, B. E. Launder, W. C. Reynolds, F. W. Schmidt, and J. H. Whitelaw, Stanford Univ., Stanford, CA, 1989, pp. 225–237.

[2]Andreopoulos, J., and Rodi, W., "Experimental Investigation of Jets in a Crossflow," *Journal of Fluid Mechanics*, Vol. 138, 1984, pp. 93–127.

[3]Karagozian, A. R., "An Analytical Model for the Vorticity Associated with a Transverse Jet," *AIAA Journal*, Vol. 24, No. 3, 1986, pp. 429–436.

[4]McMahon, H. M., Hester, D. D., and Palfrey, J. G., "Vortex Shedding from a Turbulent Jet in a Cross-Wind," *Journal of Fluid Mechanics*, Vol. 48, 1971, pp. 73–80.

[5]Heister, S. D., and Karagozian, A. R., "Gaseous Jet in Supersonic Crossflow," *AIAA Journal*, Vol. 28, No. 5, 1990, pp. 819–827.

[6]Lee, M. P., McMillin, B. K., Palmer, J. L., and Hanson, R. K., "Planar Fluorescence Imaging of a Transverse Jet in a Supersonic Crossflow," *Journal of Propulsion and Power*, Vol. 8, No. 4, 1992, pp. 729–735.

[7]Hartfield, R. J., Hollo, S. D., and McDaniel, J. C., "Experimental Investigation of a Supersonic Swept Ramp Injector Using Laser-Induced Iodine Fluorescence," *Journal of Propulsion and Power*, Vol. 10, No. 1, 1994, pp. 129–135.

[8]Hollo, S. D., McDaniel, J. C., and Hartfield, R. J., "Quantitative Investigation of Compressible Mixing: Staged Transverse Injection into Mach 2 Flow," *AIAA Journal*, Vol. 32, No. 3, 1994, pp. 528–534.

[9]Gruber, M. R., Nejad, A. S., Chen, T. H., and Dutton, J. C., "Mixing and Penetration Studies of Sonic Jets in a Mach 2 Freestream," *Journal of Propulsion and Power*, Vol. 11, No. 2, 1995, pp. 315–323.

[10]Waitz, I. A., Marble, F. E., and Zukoski, E. E., "Investigation of a Contoured Wall Injector for Hypervelocity Mixing Augmentation," *AIAA Journal*, Vol. 31, No. 6, 1993, pp. 1014–1021.

[11]Aso, S., Tannou, M., Maekawa, S., Okuyama, S., Ando, Y., Yamane, Y., and Fukuda, M., "A Study on Mixing Phenomena in Three-Dimensional Supersonic Flow with Circular Injection," AIAA Paper 94-0707, Jan. 1994.

[12]McMillin, B. K., Palmer, J. L., Seitzman, J. M., and Hanson, R. K., "Two-Line Instantaneous Temperature Imaging of NO in a SCRAMJET Model Flowfield," AIAA Paper 93-0044, Jan. 1993.

[13]Hermanson, J. C., and Winter, M., "Mie Scattering Imaging of a Transverse, Sonic Jet in Supersonic Flow," *AIAA Journal*, Vol. 31, No. 1, 1993, pp. 129–132.

[14]VanLerberghe, W. M., "Large-Scale Structure and Mixing in a Sonic Transverse Jet Injected into a Supersonic Crossflow," Ph.D. Dissertation, Dept. of Mechanical and Industrial Engineering, Univ. of Illinois at Urbana–Champaign, IL, Sept. 1995.

[15]Gruber, M. R., Nejad, A. S., Chen, T. H., and Dutton, J. C., "Compressibility Effects in Supersonic Transverse Injection Flowfields," *Physics of Fluids*, Vol. 9, No. 5, 1997, pp. 1448–1461.

[16]Schadow, K. C., Wilson, K. J., and Lee, M. J., "Enhancement of Mixing in Reacting Fuel-Rich Plumes Issued from Elliptical Nozzles," *Journal of Propulsion and Power*, Vol. 3, No. 2, 1987, pp. 145–149.

[17]Ho, C., and Gutmark, E., "Vortex Induction and Mass Entrainment in a Small-Aspect-Ratio Elliptic Jet," *Journal of Fluid Mechanics*, Vol. 179, 1987, pp. 383–405.

[18]Gutmark, E., Schadow, K. C., and Wilson, K. J., "Noncircular Jet Dynamics in Supersonic Combustion," AIAA Paper 87-1878, June 1987.

[19]Schadow, K. C., Gutmark, E., Koshigoe, S., and Wilson, K. J., "Combustion-Related Shear-Flow Dynamics in Elliptic Supersonic Jets," *AIAA Journal*, Vol. 27, No. 10, 1989, pp. 1347–1353.

[20]Gutmark, E., Schadow, K. C., and Bicker, C. J., "Mode Switching in Supersonic Circular Jets," *Physics of Fluids A*, Vol. 1, No. 5, 1989, pp. 868–873.

[21]Glawe, D. D., Samimy, M., Nejad, A. S., and Chen, T. H., "Effects of Nozzle Geometry on Parallel Injection into a Supersonic Flow," *Journal of Propulsion and Power*, Vol. 12, No. 6, 1996, pp. 1159–1168.

[22]Glass, D. R., "Effects of Acoustic Feedback on the Spread and Decay of Supersonic Jets," *AIAA Journal*, Vol. 6, No. 10, 1968, pp. 1890–1897.

[23]Gruber, M. R., Nejad, A. S., Chen, T. H., and Dutton, J. C., "Bow Shock/Jet Interaction in Compressible Transverse Injection Flowfields," *AIAA Journal*, Vol. 34, No. 10, 1996, pp. 2191–2193.

[24]Gruber, M. R., Nejad, A. S., Chen, T. H., and Dutton, J. C., "Large Structure Convection Velocity Measurements in Compressible Transverse Injection Flowfields," *Experiments in Fluids*, Vol. 22, No. 5, 1997, pp. 397–407.

[25]Gruber, M. R., and Nejad, A. S., "New Supersonic Combustion Research Facility," *Journal of Propulsion and Power*, Vol. 11, No. 5, 1995, pp. 1080–1083.

[26]Hartman, J. R., Famil-Ghiriha, J., Ring, M. A., and O'Neal, H. E., "Stoichiometry and Possible Mechanism of SiH_4-O_2 Explosions," *Combustion and Flame*, Vol. 68, No. 1, 1987, pp. 43–56.

[27]Rogers, R. C., Weidner, E. H., and Bittner, R. D., "Quantification of Scramjet Mixing in the Hypervelocity Flow of a Pulse Facility," AIAA Paper 94-2518, June 1994.

[28]Samimy, M., and Lele, S. K., "Motion of Particles with Inertia in a Compressible Free Shear Layer," *Physics of Fluids A*, Vol. 3, No. 8, 1991, pp. 1915–1923.

[29]Glawe, D. D., Samimy, M., Nejad, A. S., and Chen, T. H., "Effects of Nozzle Geometry on Parallel Injection from Base of an Extended Strut into a Supersonic Flow," AIAA Paper 95-0522, Jan. 1995.

[30]Keffer, J. F., and Baines, W. D., "The Round Turbulent Jet in a Cross-Wind," *Journal of Fluid Mechanics*, Vol. 15, 1963, pp. 481–496.

[31]McDaniel, J. C., and Graves, J., "Laser-Induced Fluorescence Visualization of Transverse Gaseous Injection in a Nonreacting Supersonic Combustor," *Journal of Propulsion and Power*, Vol. 4, No. 6, 1988, pp. 591–597.

[32]Rothstein, A. D., and Wantuck, P. J., "A Study of Normal Injection of Hydrogen into a Heated Supersonic Flow Using Planar Laser-Induced Fluorescence," AIAA Paper 92-3423, July 1992.